

Transertion and cell geometry organize the *Escherichia coli* nucleoid during rapid growth

Christoph Spahn^{1,2*}, Stuart Middlemiss³, Estibaliz Gómez-de-Mariscal⁴, Ricardo Henriques^{4,5},
Helge B. Bode^{2,6,7,8,9}, Séamus Holden^{3,10}, Mike Heilemann^{1*}

¹ Institute of Physical and Theoretical Chemistry, Goethe-University Frankfurt, Frankfurt, Germany

² Department of Natural Products in Organismic Interaction, Max Planck Institute for Terrestrial Microbiology, Marburg, Germany

³ Centre for Bacterial Cell Biology, Newcastle University Biosciences Institute, Faculty of Medical Sciences, Newcastle upon Tyne NE24AX, United Kingdom

⁴ Instituto Gulbenkian de Ciência, 2780-156 Oeiras, Portugal

⁵ MRC-Laboratory for Molecular Cell Biology, University College London, London, UK

⁶ Molecular Biotechnology, Department of Biosciences, Goethe-University Frankfurt, 60438 Frankfurt, Germany

⁷ Center for Synthetic Microbiology (SYNMIKRO), Phillips University Marburg, 35043 Marburg, Germany

⁸ Senckenberg Gesellschaft für Naturforschung, 60325 Frankfurt, Germany

⁹ Department of Chemistry, Phillips University Marburg, 35043 Marburg, Germany

¹⁰ School of Life Sciences, University of Warwick, Gibbet Hill Campus, Coventry, UK

* Corresponding authors

Christoph Spahn (lead contact): Christoph.spahn@mpi-marburg.mpg.de

Mike Heilemann: heilemann@chemie.uni-frankfurt.de

ABSTRACT

Using 3D single-molecule localization microscopy and live-cell imaging, we show that the *Escherichia coli* nucleoid adopts a condensed, membrane-associated configuration during rapid growth. To study the influence of different biosynthetic processes on nucleoid morphology and positioning, we recorded multi-colour super-resolution images during drug treatment. After developing analysis routines for confocal and super-resolution images, we captured highly resolved snapshots which revealed the complete loss of the membrane-bound state of the nucleoid within 10 minutes of halting transcription and translation. This indicates an active role of transertion (coupled transcription, translation and membrane insertion) in nucleoid organization. In contrast, cell wall synthesis inhibition only affects nucleoid organization during morphological changes. Further, we provide evidence that the *E. coli* nucleoid spatially correlates with MreB in unperturbed *E. coli* cells, while this correlation diminishes in cells with changed cell geometry or upon inhibition of protein biosynthesis. Replication inhibition experiments, as well as multi-drug treatments highlight the role of entropic effects and transcription in nucleoid condensation and positioning. In summary, we provide experimental evidence for transertion as a principal organiser of the bacterial nucleoid, and show that an altered metabolic state and antibiotic treatment both lead to major changes in the degree of transertion and overall spatial organization of the nucleoid. Our high-resolution characterization reveals dynamics of antibiotic action and provides tools to quantify bacterial chromosome organization. This does not provide valuable insights into the role of transertion, but can also be applied to study other cell-biological processes.

INTRODUCTION

Chromosome replication and segregation represent the fundamental processes underlying cell proliferation and survival. In bacteria, they occur simultaneously with other cellular processes, such as transcription, translation or signalling, and share the same space due to the lack of compartmentalisation. Despite this lack of compartmentalization, bacterial chromosomes were found to be highly organized spatiotemporally, with nucleoid organization strongly differing between bacterial species¹⁻³. The entity of chromosomal DNA in a bacterial cell is called the ‘nucleoid’ and much research is dedicated to investigate its organization. Seminal work showed that the *Escherichia coli* nucleoid is not randomly floating within the cell cytosol but shows structuring into domains of varying sizes on the molecular level by the action of nucleoid-associated proteins⁴⁻⁶. Similar to eukaryotic nuclei, chromosomal regions populate specific areas in non-replicating cells and replicating nucleoids show precise intracellular positioning^{7,8}. Interestingly, the *E. coli* nucleoid exhibits varying complexity, i.e. degree of sub-structuring, depending on the nutrient availability and, thus, growth rate⁹. In particular, nucleoids are more condensed and structurally complex during fast growth than during slow growth, where it populates a larger fraction of the cytosol. The global morphology of these ‘complex’ nucleoids was found to be stable on the minute time scale, while fast imaging in slowly growing cells revealed rapid transversal nucleoid fluctuations along the entire bacterial long axis^{8,10}. Despite these large differences in organization, we still do not fully understand the molecular mechanisms that shape the nucleoid in an environment-dependent manner.

Entropy has early been identified as a key principle in chromosome organization, contributing to sister chromosome segregation, nucleoid positioning and compaction¹¹⁻¹³. Other factors involved in nucleoid organization are confinement, molecular crowding, cell size and morphology^{13,14}. Wall-less *E. coli* cells, so-called L-forms, exhibit abnormal cell and nucleoid shapes, while their growth in a confined space resulted in nucleoid morphology and chromosome segregation patterns as they are seen in walled cells¹⁵. Chromosome size and positioning was further found to scale with cell size due

to confinement and molecular crowding¹³. The correlation between cell and nucleoid size was recently extended to a wide range of bacterial species, highlighting a conserved contribution of physical principles to chromosome organization¹⁶.

In addition, various biological processes strongly influence bacterial chromosome organization. A large body of work investigated the effect of biosynthetic processes such as transcription or translation on nucleoid structure, revealing dramatic reorganization during inhibition¹⁷⁻²³. These effects are so severe that cell and nucleoid morphology can be used as a readout for drug mode-of-action studies, drug screening applications and antibiotic susceptibility testing²⁴⁻²⁶. Particularly, transcription was found to affect chromosome size and dynamics in different bacterial species as shown by Hi-C and microscopic experiments^{17,27-29}. Inhibition of translation or DNA replication also leads to strong nucleoid phenotypes, indicating that chromosome organization is tightly connected to biosynthetic processes^{17-19,21}. Of note, nucleoid reorganization by transcription- and translation-halting drugs occurs on a rapid time scale, as e.g. shown by Bakshi and colleagues¹⁸. This provided evidence that spatiotemporal coupling of transcription, translation and insertion of membrane proteins, so-called transertion, keeps the nucleoid in an expanded state^{18,20}. Localized protein biosynthesis increases efficiency and is conserved in eukaryotic cells, in which proteins are co-translationally translocated into the endoplasmic reticulum³⁰. As transcription in bacteria often occurs co-translationally³¹, an indirect coupling of the nucleoid to the membrane represents an attractive hypothesis^{32,33}. In fact, passive segregation by membrane attachment of the origin of replication together with cell elongation was one of the first proposed mechanisms for bacterial chromosome segregation³⁴. The observation of rapid re-centring of nucleoids in asymmetrically dividing cells, however, highlights entropy as the driving force behind chromosome positioning¹⁵. While transertion could just be a consequence of co-transcriptional translation in a highly confined space, it was recently shown to be important for the assembly of bacterial secretion systems³⁵.

While many studies investigated the effect of individual processes on bacterial chromosome organization, there is little work on synergistic effects. In addition, most microscopic work uses diffraction-limited approaches and do not take advantage of the benefit provided by super-resolution microscopy, in particular single-molecule localization microscopy (SMLM)^{36,37}. We thus sought to study *E. coli* nucleoid organization at high resolution during unperturbed growth and drug treatment. We chose rapidly growing cells to investigate the highly complex and structured nucleoid⁹ and to reveal the mechanisms that mediate this organization. SMLM showed a condensed nucleoid positioned close to the inner membrane, which we could verify in live cells. To investigate the nature of this organization, we chemically fixed bacteria at different time points during inhibition of cell wall synthesis, transcription, translation, protein translocation and DNA replication. Perturbation of cell wall synthesis highlighted the membrane-bound state of the nucleoid. Inhibition of transcription or translation, on the other side, resulted in a complete nucleoid detachment from the membrane within the time scale of 2-10 minutes, strongly indicating transertion as the mechanism behind the observed nucleoid anchoring. By reversibly arresting DNA replication, we further observe that nucleoids locate at the cell centre of elongating cells and rapidly repopulate DNA-free areas after release from replication block. This happens faster than cell elongation, highlighting the role of cell geometry and entropy in nucleoid positioning and expansion. Together, our work shows that transertion determines the three-dimensional configuration of the *E. coli* nucleoid during fast growth, while nucleoid positioning is mainly mediated by entropic effects.

RESULTS

The nucleoid in fast-growing *E. coli* is condensed and tethered to the membrane

Previous studies suggested that the nucleoid in fast-growing *E. coli* possesses a helical or twisted configuration^{6,9,10}. To investigate this at high spatial resolution, we metabolically labelled DNA in *E. coli* cells growing at a mass doubling time of 27 min using 5-ethynyl-2-deoxyuridine (EdU)³⁸. We labelled these cells Alexa-Fluor 647 via click chemistry, which allows for high-resolution 3D single-molecule imaging (**Fig. 1A**) due to the superior brightness of this fluorophore. 3D imaging revealed a condensed, ring-like nucleoid structure with a clear DNA-free centre in the cross-section (**Fig. 1A iii and iv, Supplementary Video 1**). This arrangement was not seen in the 2D projection (**Fig. 1A i**), highlighting that projection effects in widefield and 2D SMLM images might not reveal the actual organization of the target structure^{7,39}. In the 3D image, the nucleoid appears positioned close to the cell membrane, as we have previously shown using STED microscopy⁴⁰. As recent studies suggest that transesterification affects the positioning of genetic loci and nucleoid structuring⁴¹, we co-imaged the nucleoid with MreB, which is part of an essential, abundant and exclusively membrane-associated multi-protein complex. As copper-catalysed click-labelling destroys fluorescent proteins, we used transiently binding labels and performed dual-color point accumulation for imaging in nanoscale topography (PAINT) in cells expressing an MreB^{sw}-sfGFP protein fusion^{22,42}. To increase the resolution, we deconvolved 3D stacks of the MreB fusion (**Fig. S1**) and registered the resulting image with the highly-resolved PAINT images. Pseudo-3-color imaging in the same spectral channel (see methods) using MreB-sfGFP^{sw}, JF₅₀₃-Hoechst and Potomac Gold suggests a moderate degree of spatial correlation between elongasomes and the nucleoid, which is investigated in this study.

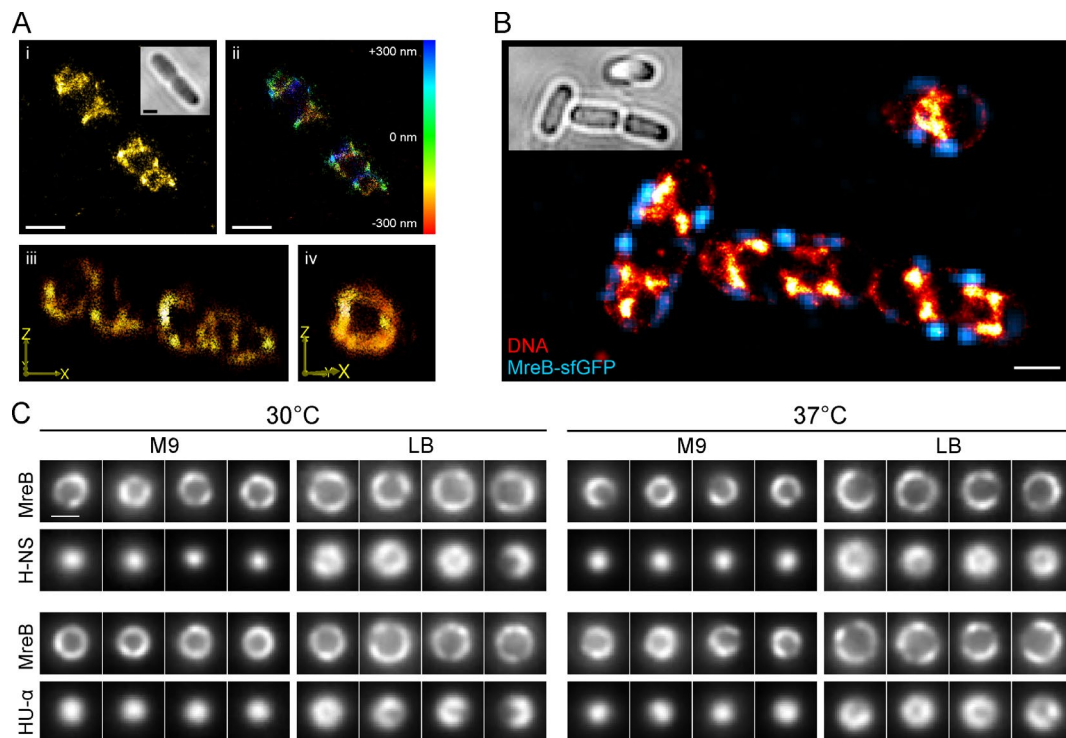


Figure 1: The nucleoid of fast-growing *E. coli* positions along the inner membrane. [A] 3D dSTORM images of a metabolically labeled (EdU, clicked with Alexa Fluor 647), chemically fixed cell shown as 2D projection (i), color-coded by depth (ii) and tilted 3D views (iii and iv). [B] 2D PAINT image of the nucleoid and membrane (red hot) of a fixed NO34 cell expressing an MreB^{sw}-sfGFP fusion (deconvolved, cyan). [C] Live-cell VerCINI^{43,44} measurements of *E. coli* cells expressing MreB^{sw}-sfGFP and H-NS/HU- α -mScarlet-1 fusions. Nucleoids are condensed in the radial cell centre when cells are grown in M9 ($t_d \sim 100$ min), but close to the membrane during fast growth in LB ($t_d \sim 27$ min). Scale bars are 1 μ m (A, B) and 500 nm (C).

To exclude fixation artefacts and validate that the membrane-proximal nucleoid arrangement exists *in vivo*, we created *E. coli* strains that express an H-NS-mScarlet-I or HU- α -mScarlet-I protein fusion in the MreB^{SW}-sfGFP background (**Table S1**). To obtain images of cross-sections, we imaged these strains in vertical orientation using the VerCINI approach (**Fig. 1C**)^{43,44}. While the nucleoid is positioned at the radial cell centre during slow growth (M9, $t_d \sim 120$ min), it locates at the periphery during rapid growth, both at 30°C and 37°C ($t_d \sim 25$ -30 min). We thus deduced that the highly wound arrangement and membrane-proximal positioning is a feature of the *E. coli* nucleoid during rapid growth. The increased nucleoid complexity at faster growth is in agreement with previous studies, so is the centred positioning of an elongated nucleoid during slow growth^{9,10}. We also performed live-cell imaging of these strains using confocal laser-scanning microscopy (CLSM), which showed nucleoid dynamics on the second time scale and a stable nucleoid positioning at the cells' quarter positions (**Supplementary Videos 2 and 3**). Global nucleoid positioning hereby coincided with MreB distribution (**Fig. S2**).

Inhibition of cellular processes alters nucleoid organization

To study the basis of the observed membrane-proximal positioning, we treated exponentially growing *E. coli* cultures with antibiotics that inhibit specific steps in biosynthetic pathways (**Fig. 2, Table S2**). For inhibition of cell wall synthesis, we used MP265 (A22 analogue, inhibits MreB polymerization)⁴⁵ and Mecillinam (PBP2 inhibitor, inhibits peptidoglycan transpeptidation)⁴⁶. Protein biosynthesis was inhibited using high concentrations of rifampicin (transcription inhibition) and chloramphenicol (translation inhibition)^{18,47}. Additionally, we perturbed protein translocation (sodium azide) and DNA replication (nalidixate, DNA gyrase and topoisomerase IV inhibitor). Each antibiotic was added to the *E. coli* culture during mid-log phase ($OD_{600} \sim 0.25$) and aliquots were chemically fixed at defined time points, labelled for DNA and membranes and imaged by CLSM (**Fig. 2A**). Over the time course of 60 minutes during unperturbed growth, the nucleoid shows the expected sub-structuring and positioning at quarter positions (**Fig. 2B**)^{9,38}. Both MP265 and Mecillinam treatments induced a rod-to-sphere transition with significant cell rounding occurring after 30 min. Interestingly, inhibition of MreB polymerization with MP265 led to the rapid formation of polar foci or aggregates that were most prominent in the first 2-10 minutes of treatment and successively disappeared with ongoing MP265 exposure. Azide treatment did not show apparent changes in nucleoid morphology, but increasing MreB aggregation at 30-60 min exposure. When we inhibited protein biosynthesis, changes in nucleoid morphology were more dramatic. Both inhibition of transcription (rifampicin) and translation (chloramphenicol) led to an instant contraction of the nucleoid in the first minutes, in line with previous work¹⁸. While nucleoids started to expand after ~ 10 -20 minutes of rifampicin treatment, condensation continued in chloramphenicol-treated cells. Stalling of replisomes by the gyrase inhibitor nalidixate led to nucleoid positioning at the cell centre, while cells continued to grow and formed large, nucleoid-free areas. MreB hereby populated the entire cell cylinder and facilitated elongation also in nucleoid-free regions.

To assess global changes induced by the different antibiotics, we developed an image analysis routine that provides heat maps of the nucleoid and MreB (**Fig. 3**). For this purpose, we extracted individual cells from CLSM images and processed these images by straightening, alignment, normalization and finally averaging (**Fig. 3A, i**). The resulting image represents the average cell for the specific condition (antibiotic treatment and exposure time), which we term 'population average' throughout this study.

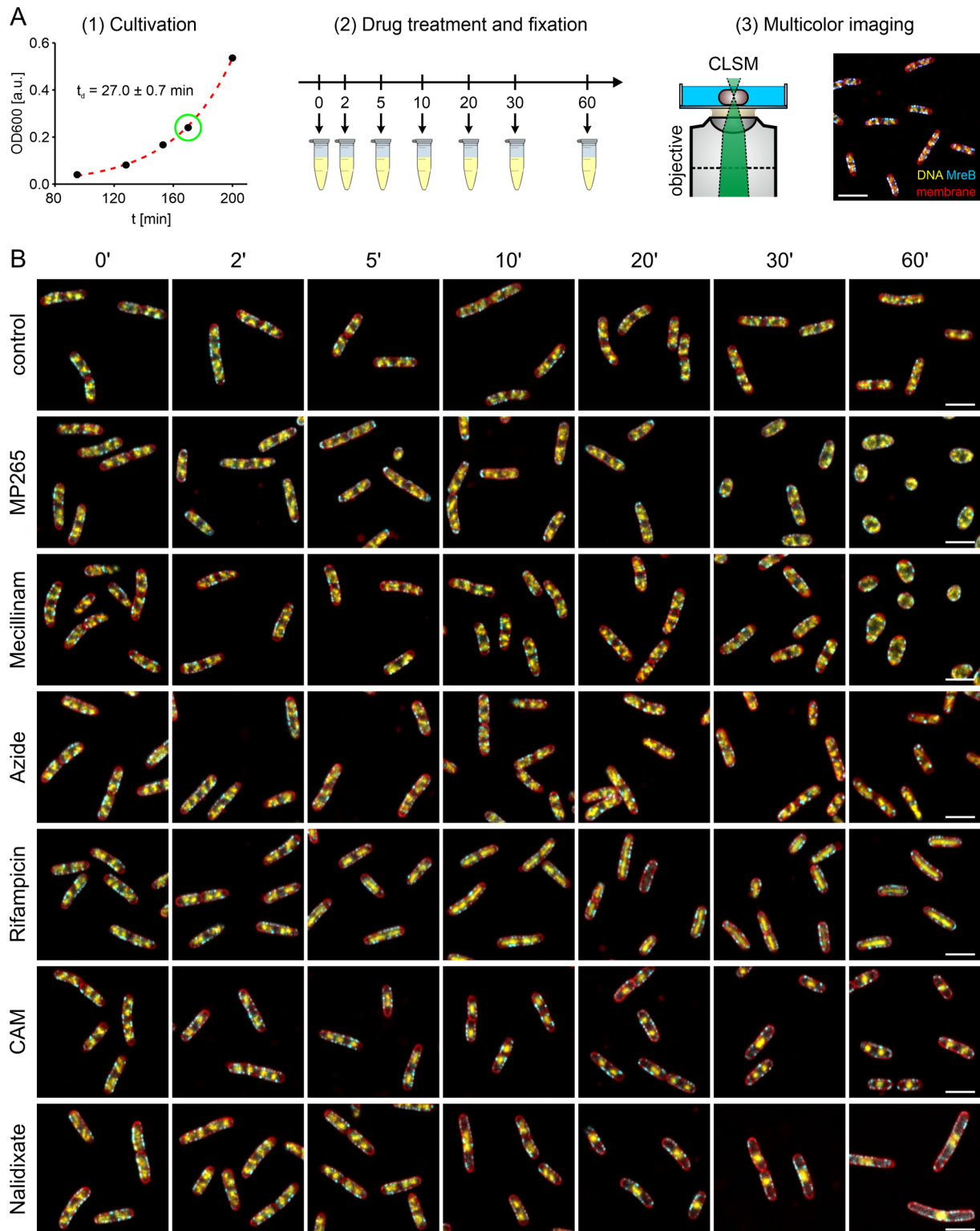


Figure 2: Cell fixation allows capturing antibiotic action dynamics at the minute time scale. [A] Schematic of the experimental design. Cells were grown in LB to exponential phase ($t_d \sim 27$ min), antibiotics were added and aliquots were chemically fixed at distinct time intervals. Bacteria were then immobilized, stained for DNA (DAPI, yellow hot) and membranes (Nile Red, red) and imaged using CLSM. Chromosomally expressed MreB-sfGFP^{sw} is shown in cyan. [B] Representative images of bacteria treated with different antibiotics for specific time intervals. CAM = Chloramphenicol. Scale bars are 3 μ m.

For quantitative analysis, we measure the relative nucleoid length (RNL) in individual cells (Fig. 3A, ii). RNL describes the fraction of cell length that is populated by chromosomal DNA. This metric is similar

to the relative nucleoid size used by Cabrera and colleagues⁴⁷, yet we prefer RNL in diffraction-limited images due to the 2D projection effects shown in **Figure 1A** and literature^{7,39}. To monitor reorganization of MreB following antibiotic treatment, we quantified its relative distribution at the cell cylinder and cell poles (**Fig. 3A, iii**). The latter are typically avoided by MreB, likely due to a combination of processive elongasome-driven motion of MreB and spontaneous alignment of curved MreB filaments circumferentially around the cell sidewall⁴⁸. Population averages of the drug treatments validate the observations made in **Fig. 1**. Untreated cultures showed two bilobed sister chromosomes, as it is expected under fast-growing conditions (**Fig. 3B**)⁹. While population averages hide length-dependent effects, the existence of two nucleoids and the global positioning at quarter positions was observed for all length intervals (**Fig. S3**). Upon inhibition of MP265 and mecillinam treatment, changes in nucleoid positioning and morphology only appeared during rod-to-sphere transition, while apparently, no changes were observed during short drug exposure. To assess global changes in nucleoid organization, we measured the long and cross-axis profiles in population averages (**Fig. S4 – S8**). Polar recruitment of MreB during MP265 treatment is clearly visible in length axis plots (**Fig. S4**) and was strikingly consistent for both replicates. Concomitant with cell rounding, the bilobed nucleoid distribution diminished for both MP265 and Mecillinam treatment (**Fig. S4**). Here, cross-axis plots did not reveal strong reorganization along the bacterial short axis (**Fig. S5**).

For the inhibition of protein biosynthesis, population averages revealed severe changes in nucleoid morphology. Inhibition of protein translocation with sodium azide only induced MreB clustering at long exposure times, while global nucleoid organization was not affected (**Fig. 3B, S6 and S7**). When inhibiting transcription (rifampicin) or translation initiation (chloramphenicol), population averages show an abrupt nucleoid condensation along the bacterial long axis. Nucleoids expand again after 5 min rifampicin exposure, while they continue condensing during chloramphenicol treatment (**Fig. 3B and S6**). Cross-axis plots further showed that nucleoids also contract along the short axis. This effect is stronger for rifampicin treatment than for chloramphenicol (**Fig. 3B and S7**).

RNL measurements (**Fig. 3C**) and analysis of MreB intensity distribution (**Fig. 3D**) confirmed our observations made by visual inspection. In particular, RNL analysis showed a maximal longitudinal nucleoid condensation in rifampicin-treated cells after 5 min, while it plateaued at 30 min in CAM-treated cultures. Other treatments did not show severe changes in RNL. Of note, we did not observe changes in control cultures (**Fig. 3C, Fig. S8**), which showed a constant RNL of 0.64 ± 0.02 (s.d.) throughout the time course of 1 h. The RNL at $t = 0$ min for all treatments was also reproducible with an average value of 0.65 ± 0.04 (s.d., $n = 12$). MreB distribution analysis revealed maximal polar localization after 5 min of MP265 treatment, which declined gradually with continuous exposure time as observed previously⁴⁹. This effect was also observed in live cells immobilized under MP265-containing agarose pads (**Supplementary Video 4**). However, drug treatment dynamics were delayed under agarose pads, likely due to the change in temperature (25°C vs 32°C), lack of agitation, or partial drug inactivation during its addition to warm LB-agar. To exclude artefacts induced by cell density or length, we analysed the MreB distribution in population averages of the control culture and for specific length intervals (**Fig. S9**). Both controls showed a constant MreB intensity distribution, with most signals being detected in the cylindrical part of the average cell. Interestingly, inhibition of PG crosslinking using mecillinam also induced a slight reorganization of MreB towards the cell poles (**Fig. 3D**). This indicates that MreB polymerization might be coupled to the action of PBP2. Perturbation of protein synthesis or translocation led to a gradual shift of MreB towards the poles. As MreB localisation coincides with nucleoid distribution along the bacterial long axis, we additionally blocked DNA gyrase using nalidixate, which is known to stall DNA replication (**Fig. 3E**). Consistent with previous work, this led to a mid-cell-positioned nucleoid while cell growth continued, resulting in a continuous

drop in RNL (**Fig. 3E, Fig. S11**)²¹. The average nucleoid length hereby decreased within the first 20 min, caused by division of cells with already separated sister chromosomes (**Fig. S10**).

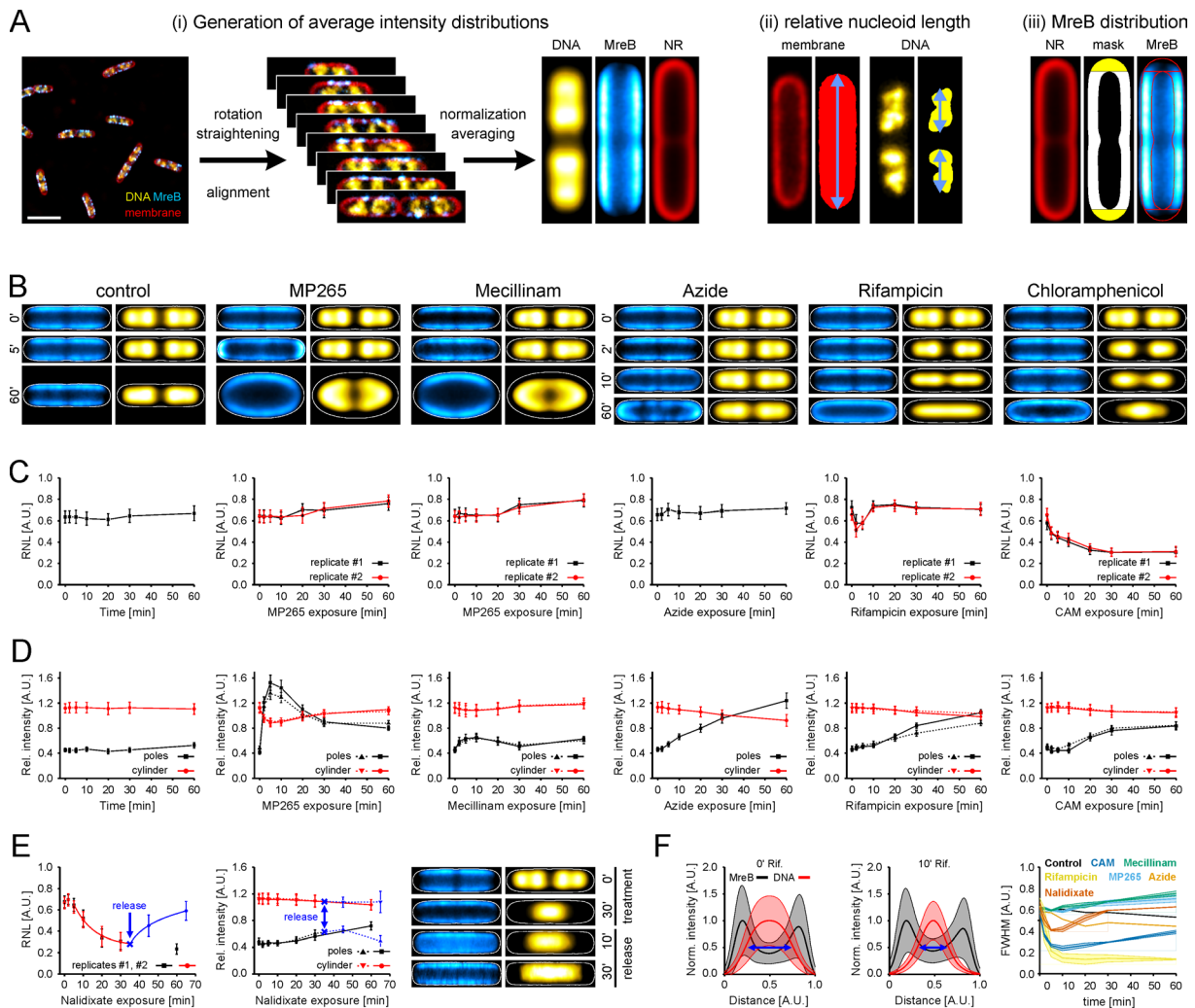


Figure 3: Analysis of drug-treated *E. coli* cells on the population and single-cell level. [A] Analyses performed with CLSM images. Schematic of the generation of population average images (i): Bacterial cells are detected in confocal images, rotated, straightened and aligned. After normalisation by cell length and width, cells are averaged at each time point, generating a population average image (see methods). NR = Nile red. DNA distribution along the bacterial long axis was determined on the single cell-level by measuring the nucleoid length relative to the cell length (ii). (iii) Quantification of MreB distribution: Polar (yellow) and cylindrical sections (white) were segmented in population average images and the relative MreB intensity was calculated. **[B]** Population average images of selected time points. Cell outlines (white lines) were obtained from membrane average images. **[C]** Relative nucleoid length and **[D]** MreB intensity distributions of antibiotic treatments shown in **[B]**. **[E]** Relative nucleoid length (left), MreB intensity distribution (middle) and selected population averages (right) of replication arrest and release using nalidixate. **[F]** Determination of the average nucleoid width using population average intensity distributions. Shown are exemplary cross-axis plots without treatment (left) and 10 min rifampicin treatment (middle). The full-width at half maximum (FWHM, blue arrows) was determined by integrating the intensity distribution. FWHM over treatment time differ for antibiotic treatments (right). Error bars in **[B]** and **[E]** (left plot) represent the standard deviation and in **[D]** and **[E]** (right plot) the standard error of the mean. Control and azide treatment experiments were only performed once. Shaded areas in **[F]** represent standard deviations (left and middle plot: pixel-wise standard deviation of population average images; right plot: standard deviation of two replicates). Lines in **C**, **D** and **E** are added for visualisation purpose and do not refer to an underlying model. Scale bar in **[A]** is 3 μm .

To track the cellular response upon the continuation of chromosome replication, we removed nalidixate in one replicate after 30 min treatment by washing cells twice with fresh LB. This resulted in a fast increase in RNL following a logarithmic function (**Fig. 3E**, blue points and line, **Fig. S11**).

Finally, we quantified nucleoid distribution along the bacterial cross-axis by determining the full-width at half maximum (FWHM) in intensity plots of population averages (**Fig. 3F**). Nucleoids contracted rapidly during rifampicin and chloramphenicol treatment, reaching a maximal condensation after 5 – 10 min, while other treatments showed only minor changes over time.

Super-resolution microscopy reveals complete nucleoid detachment from the inner membrane upon inhibition of protein biosynthesis

Recent advances in super-resolution imaging allow visualizing the nucleoid in individual cells at ~ 30 nm resolution^{22,50}. We used transiently binding fluorophores Nile Red and JF₆₄₆-Hoechst in Point Accumulation for Imaging in Nanoscale Topography (PAINT)⁵¹ to provide highly resolved snapshots of drug-treated cells (**Fig. 4**). Additional cells of different lengths for all treatments are provided in **Fig. S14 – S19**. From these super-resolved images, we quantified the subcellular nucleoid distribution by analytically determining the relative DNA content in consecutive radial layers reaching from the cell periphery (membrane) towards the cell centre (**Fig. 4A**). We term the resulting distribution the radial intensity distribution (RID) of the nucleoid.

In agreement with our previous work, super-resolved nucleoids of untreated cells were bilobed and sub-structured, avoiding the cell poles and spanning the entire width of the bacterial cell (**Fig. 4B**). This image represents the 2D projection of the membrane-proximal nucleoid positioning observed in **Fig. 1**. Multi-colour PAINT imaging in cells expressing H-NS-mScarlet-I shows a complete overlap of H-NS and PAINT signals, confirming that we image the entire nucleoid (**Fig. S12**). Image acquisition with an alternative commercial microscope for super-resolution imaging (Zeiss Elyra PS1) (**Fig. S13**) led to similar results. Together with live-to-fixed controls that we performed in previous work²², we are confident that we capture snapshots of the native nucleoid organization occurring in live *E. coli* cells.

The rod-to-sphere transition induced by perturbation of cell wall synthesis resulted in widened cells with expanded nucleoids. This reduces the effect of 2D projection compared to untreated cells, as the DNA is distributed within a larger axial range while the observed cross-section remains constant (see **Supplementary Note 1**). Positioning of chromosomal DNA close to the membrane thus becomes more evident (**Fig. 4B**, MP265 and Mecillinam, 30' and 60'). In contrast to untreated cells (t = 0 min), the nucleoid also populated the cell poles, indicating that cell geometry affects nucleoid positioning. As observed in confocal images (**Figs. 2 and 3**), treatment with sodium azide did not lead to global nucleoid reorganization. Next to MreB aggregation, nucleoids appeared to be slightly less condensed, which might be attributed to a reduced activity of SMC complexes upon de-energization. Specific inhibition of SecA by sodium azide explains MreB reorganization, as a similar MreB mislocalization was recently observed in SecA-defective cells⁵². PAINT images of rifampicin- and chloramphenicol-treated cells visualized the instant collapse of the nucleoid upon inhibition of protein biosynthesis (**Fig. 4B**). Here, nucleoids remained partially attached to the membrane within the first minutes (**Fig. 4B**, **Figs. S17 and S18**, 2 min), while they were completely detached after 10 min of treatment. Interestingly, the loss of nucleoid fine structure also appeared on the minute timescale, suggesting that entropic effects such as depletion attraction and nucleoid occlusion might play a significant role. Super-resolved snapshots of nalidixate-treated cells showed that the mid-cell stalled nucleoid remains associated with the inner membrane (**Fig. 4B**).

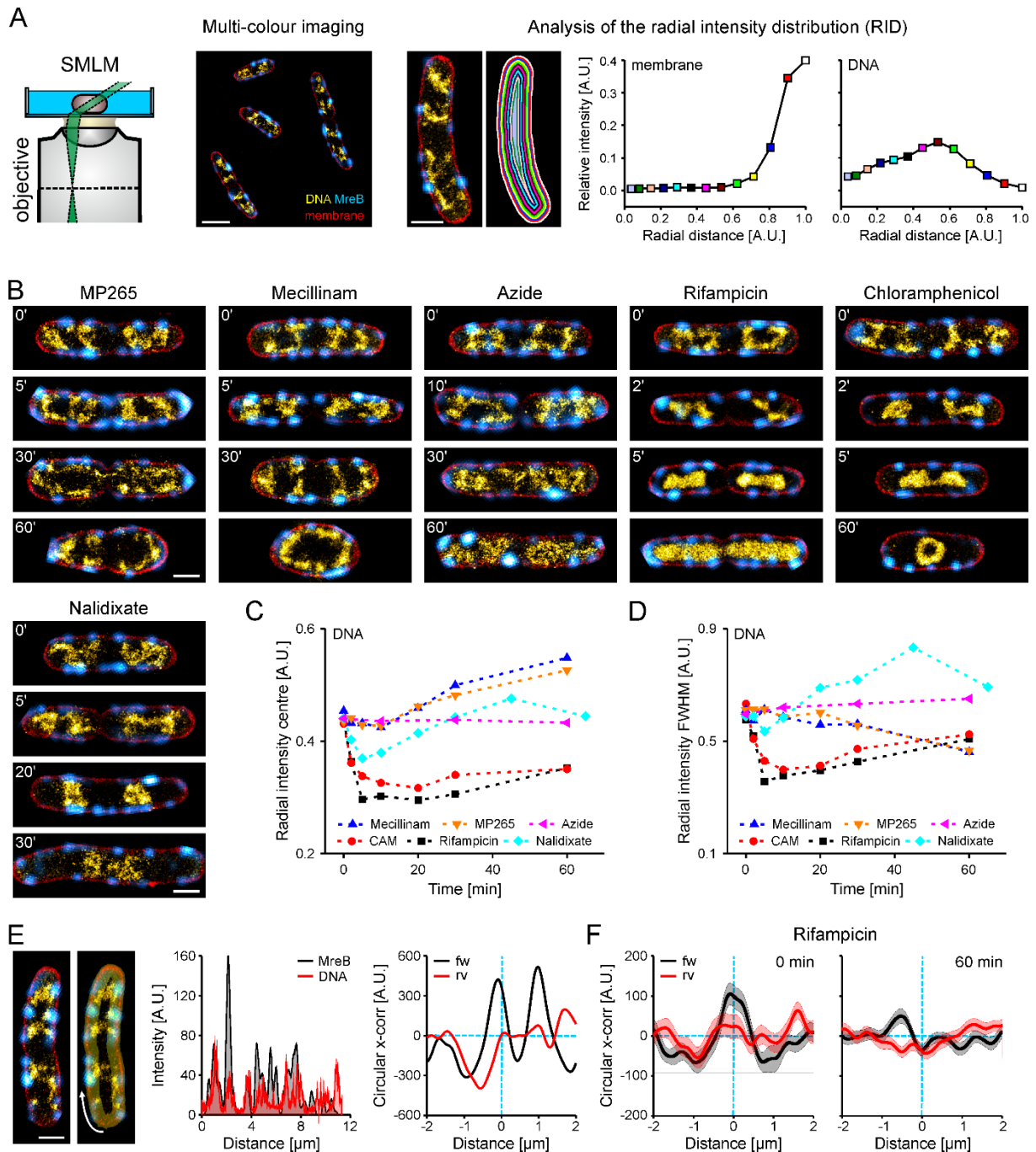


Figure 4: Super-resolution imaging reveals complete membrane detachment during inhibition of transcription and translation. [A] Schematic of multicolor imaging (left) of MreB (cyan), membrane (red) and DNA (yellow hot), as well as RID analysis (right). Cells are segmented into radial slices based on the membrane channel and the relative intensity is determined for each slice. Relative area indicates the distance from cell periphery (1) to the radial cell center (0). A chloramphenicol-treated cell (60 min) is shown as example. [B] Representative images of different time points during drug treatment. [C] Plot of RID center of masses vs. drug exposure. [D] Plot of RID FWHM vs. drug exposure. [E] Circular cross-correlation of MreB and DNA signal reveals non-random proximity. Intensities are measured along the perimeter of the cell (yellow transparent area and white arrow, left panel). Intensity plots of MreB (black) and DNA (red) of the shown cell (mid panel). Plot of circular cross-correlation (x-corr) with respect to the lag distance. Cross-correlation was calculated for the actual intensity traces (fw, black line) and with one inverted intensity trace (rv, red line) for randomization. Light blue dashed lines indicate the zero values of the x- and y-axis. [F] Averaged circular cross-correlation for untreated and rifampicin-treated (60 min) cells. Lines and data points represent mean values and the shaded area the standard errors of the mean. Scale bars are 1 μ m.

Release from replication block resulted in structured, strongly elongated nucleoids with membrane-proximal positioning along the entire cell cylinder (**Fig. S19**). To compare the changes in nucleoid organization, we calculated the RID for all treatments and time points (**Fig. S20**) and extracted the centre of mass of the intensity distribution (**Fig. 4C**) as well as the distribution width (FWHM) (**Fig. 4C**). In agreement with CLSM results, rifampicin and chloramphenicol had the strongest effect on nucleoid arrangement with a rapid shift of the DNA distribution towards the radial cell centre and a strong decrease in FWHM within the first 10 minutes. Cell widening upon MP265 and mecillinam exposure led to a shift of DNA signal towards the cell periphery and a narrowing of the radial intensity distribution, both attributed to the reduced effects of 2D projection (**Fig. 4C/D, Fig. S20**).

Our super-resolved images surprisingly showed qualitative evidence for a moderate association of chromosomal DNA with MreB (**Fig. 1B, Fig. 4, Figs. S12-S19**). To test whether the apparent spatial correlation between the nucleoid and MreB is random or specific, we developed a circular cross-correlation approach using intensity traces of two channels measured along the cell perimeter (**Fig. 4E**). In the example cell, the intensity profiles (300 nm line width) of MreB and DNA signals overlap to a large extent. (**Fig. 4E, mid panel**). Circular shifting of one intensity trace allows calculating the cross-correlation between the two signals, which we performed for lag distances between - 2 μm and 2 μm . A correlation would result in a peak centred at a lag distance of 0, while this peak would be absent in a random intensity distribution. We simulated the latter by reversing one intensity trace (rv), which should result in a loss of correlation. Indeed, we observe a peak for MreB and DNA signal, but not for the reversed DNA intensity trace (**Fig. 4E, right panel**). We further validated our method with simulations, in which we equidistantly positioned adjacent foci along a circle (**Fig. S22**). Rotation of both foci in 5° increments retains cross-correlation of the two signals, while the correlation averages out in the reversed control. Shift of only one channel resulted in a peak shift in the cross-correlation analysis. We thus assume that this method is suitable for detecting non-random association of two signals, in this case the *E. coli* nucleoid and elongasomes. Applying the method to the super-resolved images, the average circular cross-correlation showed a local maximum at the centre position for untreated cultures (**Fig. 4F, Fig. S22**). This indicates that the observed spatial correlation between the nucleoid and MreB are non-random. Inhibition of protein biosynthesis leads to the loss of correlation (**Fig. 4F, 60' rifampicin, Fig. S22**), indicating that protein expression tethers the nucleoid to the inner membrane.

Nucleoid compaction depends on active transcription, but not on cell geometry

Recent work with wall-less L-forms of *B. subtilis* showed that nucleoid positioning depends on confinement and cell geometry¹⁵. To test whether this is also the case for nucleoid compaction in *E. coli*, we inhibited protein biosynthesis in cells that had been widened by pre-treatment with MP265 using rifampicin or chloramphenicol (**Fig. 5**). As expected, cell widening reduced the effect of 2D projection, as larger parts of the nucleoid are positioned outside of the projected volume (see **Supplementary Note 1**). This leads to a shift of the RID centre of mass (CoM) from 0.41 A.U. in untreated cells to 0.53 A.U. in widened cells. Interestingly, inhibition of transcription initiation in pre-widened cells using rifampicin results in a detached nucleoid that maintains visible sub-structuring (**Fig. 5A**). This stands in contrast to elongated cells, where transcription inhibition resulted in a relatively unstructured and elongated nucleoid positioned along the bacterial long axis (**Fig. 4B**). In pre-widened cells, the RID CoM dropped from 0.53 A.U. (MP265 only) to 0.37 A.U. (MP265 + 5 min rifampicin) and 0.39 A.U. (MP265 + 10 min rifampicin), while it dropped to 0.30 A.U. for both 5 and 10 min rifampicin treatment in elongated cells. Inhibition of translation with chloramphenicol resulted in a condensed nucleoid as it is also observed in elongated cells (**Fig. 4B**). However, the positioning at

the cell centre is much more apparent in widened cells as also shown by the shift of the nucleoid signal towards the cell centre in the RID analysis (**Fig. 5B**) (CoM = 0.36 A.U. and 0.32 A.U. for 10 and 20 min chloramphenicol, respectively). To determine whether the relative nucleoid size changes with morphology, we segmented super-resolved nucleoids using a neural network that we trained on manually segmented nucleoids (see Methods). The analysis revealed that the relative nucleoid size in treated bacteria is independent of cell geometry (**Fig. 5C**).

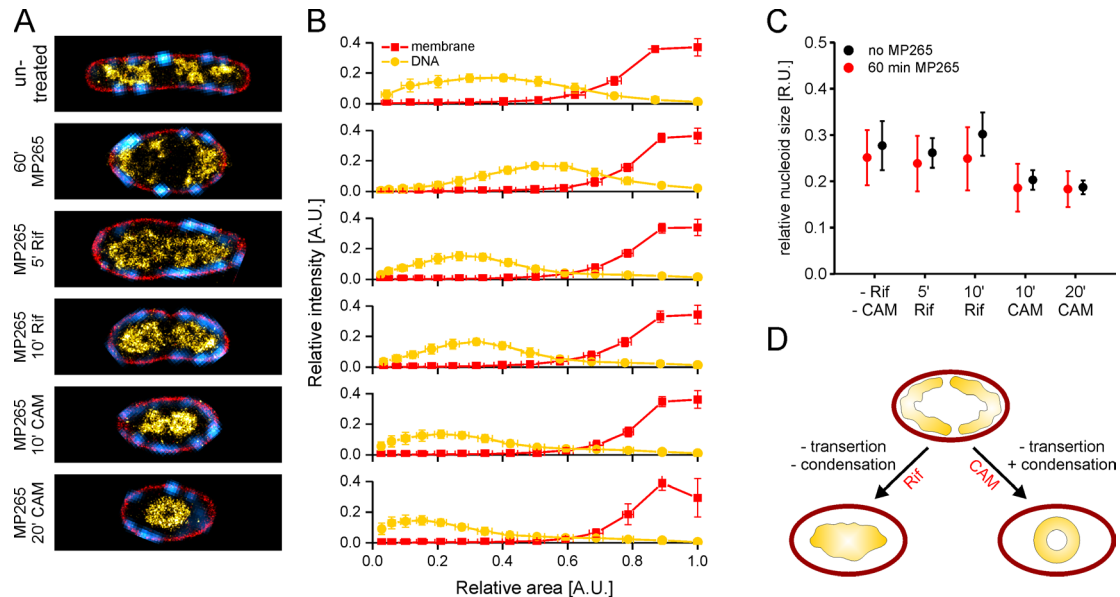


Figure 5: Inhibition of transcription and translation in widened cells. [A] Representative cells for the different conditions. **[B]** Average radial intensity distributions. **[C]** Relative nucleoid size of drug treatments in normal (no MP265, Fig. 4B) and widened cells (60 min MP265). Data points represent mean values and error bars the standard deviations. **[D]** Schematic of transcription/translation inhibition in widened cells.

This leads to a model in which nucleoid positioning depends on protein biosynthesis and entropic forces, while nucleoid compaction is mainly caused by active transcription (**Fig. 5D**)⁵³. Nucleoid size hereby seems to depend on the cell volume, as approximated by the relative nucleoid size obtained in 2D projections. To test whether cellular dimensions affect nucleoid condensation, we recorded dual-colour PAINT images of the rod-shaped Gram-negative entomopathogenic bacterium *Xenorhabdus doucetiae*. We chose this organism because it exhibits larger cellular dimensions than *E. coli*⁵⁴. In contrast to *E. coli*, the nucleoid of *X. doucetiae* cells populated the entire bacterial long axis (**Fig. 6**, untreated). However, it also detaches from the inner membrane upon rifampicin treatment, revealing a structured nucleoid similar to widened *E. coli* cells (**Fig. 5A**). Detached, but fully replicated sister chromosomes hereby remain segregated, highlighting the role of entropic forces in chromosome organization¹².

DISCUSSION

In this study, we investigated the nucleoid organization in rapidly growing *E. coli* cells during unperturbed and perturbed growth. We used confocal microscopy to visualize the global effect of various antibiotics on cell shape and nucleoid morphology and performed super-resolution microscopy measurements to provide highly resolved snapshots of drug-treated cells.

We found that the *E. coli* nucleoid is positioned in close proximity to the inner membrane during unperturbed growth in rich medium, while it occupies the radial cell centre during slow growth (**Fig. 1**). 3D single-molecule localization microscopy hereby revealed a membrane-associated nucleoid arrangement with a strikingly clear DNA-free region in the radial cell centre (**Supplementary Movie 1**). We verified this arrangement *in vivo* by imaging vertically aligned cells with VerCINI (Fig. 1C) ^{43,44}. A twisted, membrane-attached arrangement of condensed DNA was also observed in or suggested by other studies ^{6,9,10,40,55}. Fisher and colleagues hypothesized that the nucleoid represents a rigid filament in a too small cell cylinder, thus being forced into a twisted configuration ¹⁰. However, the strong and rapid reorganization observed during inhibition of protein biosynthesis (**Fig. 3**) does not support this hypothesis, unless the inhibition leads to a fast reduction in filament rigidity. Another study suggests that a condensed, donut-shaped nucleoid is thermodynamically favourable, but it does not take biosynthetic processes into consideration ⁷. Recently, a computational study showed that attractive and repulsive interactions between ribosomes and the nucleoid can cause DNA depletion at the radial cell centre, fitting the observation we made in our experiments ⁵⁶.

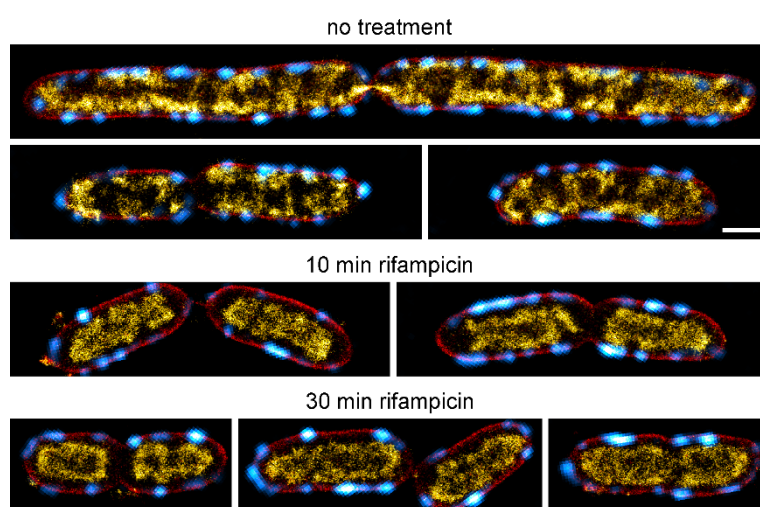


Figure 6: Nucleoid organization in the insect pathogen Xenorhabdus doucetiae. Deconvolved signal of MreB-sfGFP is shown in cyan, while super-resolved PAINT images of membranes and DNA are shown in red and yellow how, respectively. Scale bar is 1 μ m.

Our data support a model where protein biosynthesis and likely transertion couples the nucleoid to the inner membrane. This strengthens observations of previous work ¹⁸ and provides high-resolution data of nucleoid reorganization dynamics. The rapid detachment upon rifampicin and chloramphenicol treatment occurs within the first 10 minutes, a time scale that matches transcription and translation of most genes ¹⁸. The gradual detachment observed in early time points might hereby reflect the runoff of active transcription/translation events (**Fig. 4**, **Fig. S17** and **S18**). The different responses of the two treatments after a rapid contraction (**Fig. 3** and **4**) is attributed to the condensing force of active transcription and is in agreement with literature ⁵³. Notably, the observed changes in nucleoid positioning are almost binary, showing the entire DNA in membrane-proximity in widened cells and a complete detachment and centre-positioning of the nucleoid upon shutdown of protein biosynthesis (**Fig. 5**, **Fig. S21**). mRNA encoding for membrane proteins was shown to position at the inner membrane and a significant fraction of transcription is thought to happen co-translationally ⁵⁷. Although mRNA can localize to the membrane independently of translation ⁵⁸, transertion remains the most likely explanation for our observations.

Surprisingly, we found evidence of colocalization between MreB and the nucleoid. This could be mediated by previously reported interactions of MreB with EF-Tu, RNA polymerase and SecA, all

representing potential links between elongasomes and the transertion machinery^{52,59-61}. However, our data does not support an essential direct role of MreB in nucleoid anchoring, as MreB depolymerization does not affect nucleoid distribution and chromosomal DNA is not recruited to the cell poles upon MreB aggregation (**Fig. 2B**, **Fig. 3B**). Instead, we observe a strong effect of cell morphology on nucleoid distribution. Both during MP265 and mecillinam treatment, nucleoid reorganization coincides with rod-to-sphere transition (**Fig. 2**, **Fig. 3B**, **Fig. 4B**). In widened cells, chromosomal DNA is also found at polar membranes, a phenomenon that is typically not observed in rod-shaped cells (**Fig. 4**). This indicates that confinement and/or cell curvature are involved in nucleoid positioning to the quarter positions. While cell widening did not change the relative nucleoid size both during unperturbed and perturbed protein biosynthesis, it had an influence on the expansion of detached nucleoids (**Fig. 5**). Cells treated with MP265 and rifampicin showed nucleoid sub-structuring that is not visible in rod-shaped cells, in which the nucleoid shows a sausage-like arrangement along the bacterial long axis (**Fig. 4**). We attribute this observation to changes in confinement along the cells' short axis as was recently observed in L-form bacteria confined in channels of various sizes¹⁵. Increased mixing of ribosomes and the nucleoid in a larger space might also promote nucleoid expansion, but this remains to be tested by correlative imaging of ribosomes and DNA and/or single-particle tracking. A more expanded nucleoid was also observed in larger *Xenorhabdus doucetiae* cells (**Fig. 6**), supporting the hypothesis that cellular dimensions and thus confinement affects nucleoid organization.

We further observed that replication arrest by nalidixate resulted in a mid-cell-positioned nucleoid that still showed membrane-association (**Fig. 4**, **Fig. S19**). Continued cell growth led to large nucleoid-free regions that are rapidly repopulated by DNA upon removal of nalidixate (**Fig. 3E**, **Fig. S19**). The dynamics hereby exceeded the speed of cell elongation, thus suggesting entropic forces as the main cause of nucleoid expansion. This is in agreement with previous work that showed nucleoid expansion in elongating but non-replication cells as well as rapid nucleoid repositioning upon asymmetric cell division in elongated cells^{13,15}.

Next to changes in nucleoid organization, our analyses also revealed a rapid reorganization of MreB to the cell poles upon inhibition of polymerization. Work by Kawazura *et al.* showed that MreB monomers are recruited to anionic lipids, which are enriched at bacterial cell poles⁴⁹. However, we also observed subtle MreB recruitment to the cell poles during inhibition of peptidoglycan crosslinking (**Fig. 2**, **Fig. 3 B/D**) at a similar time scale. This indicates that crosslinking activity might affect MreB polymerization.

Conclusion

Our super-resolution imaging of drug-treated *E. coli* cells provides high-resolution snapshots revealing a condensed, membrane-associated configuration of the nucleoid during rapid growth. The dramatic reorganization of the nucleoid upon inhibition of protein biosynthesis, occurring within minutes, strongly implicates active transertion in maintaining this expanded, membrane-tethered state. While our data cannot conclusively demonstrate a direct role for transertion in shaping nucleoid morphology, it provides compelling evidence for transertion as a key organizing principle. By tracking the rapid response of the nucleoid to potential disruption of transertion, we have captured valuable insights into the dynamics of this process. Going forward, correlative imaging of the transertion machinery components and the nucleoid will help elucidate the molecular mechanisms underlying this phenomenon. Beyond elucidating the role of transertion, our work establishes analytical tools to quantitatively assess nucleoid organization relative to cellular landmarks like the membrane and

proteins. The automated image analysis routines we developed, including population averaging, RID analysis and circular cross-correlation, can provide versatile new approaches for investigating spatiotemporal organization in bacteria. In summary, our high-resolution snapshots of antibiotic-treated cells reveal rapid dynamics of transertion-mediated effects on nucleoid morphology, while also demonstrating broadly applicable strategies for relating subcellular structure to function.

METHODS

Bacterial strains and culturing

Bacterial strains used in this study are listed in **Table S1**. ON cultures were inoculated from single colonies into LB Lennox (5g NaCl) and grown at 32°C shaking at 200 rpm. The next day, cultures were diluted 1:200 into fresh LB and grown to exponential phase incubated at 32°C and 200 rpm. OD₆₀₀ was checked every 30 min to ensure proper growth and to determine the culture mass doubling time. The following antibiotics were added at an OD₆₀₀ of 0.25 ± 0.2: MP265 (25 µM), Mecillinam (2 µg/ml), rifampicin (100 µg/ml), chloramphenicol (50 µg/ml), sodium azide (1 mM), nalidixic acid (50 µg/ml). Antibiotic stock solutions were prepared freshly before use. In combinatorial drug experiments, 25 µM MP265 was added at OD₆₀₀ ~ 0.25, and rifampicin or chloramphenicol were added for the indicated duration at time points that sum up to 60 min total MP265 treatment. *Xenorhabdus doucetiae* was grown in LB Lennox at 30°C and 200 rpm. Similar to *E. coli*, rifampicin (100 µg/ml) was added during mid exponential phase.

Strain construction

Cloning strategies for the strains used in this study are provided in the **Supplementary Methods**. DNA fragments used for cloning were amplified by PCR using the primers listed in **Table S2**. Strains double labeled for MreB^{SW}-sfGFP and HU-α-mScarlet-I or H-NS-mScarlet-I were generated using lambda RED recombineering⁶². mScarlet-I was amplified from plasmid pmScarlet-I_C1 (Addgene # #85044)⁶³ and the chloramphenicol resistance cassette from plasmid pmMaple3-CAM (Addgene #101148)⁶⁴. Strains were verified by sequencing and fluorescence microscopy. *Xenorhabdus doucetiae* MreB^{SW}-sfGFP strain was constructed using a pDS132-based suicide plasmid⁶⁵ and the amino acid linkers (SGSS-msfGFP-SGAP) as described in Ouzounov *et al.*⁴². Due to differences in the amino acid sequence of MreB, SGSS-msfGFP-SGAP was inserted between T228 and D229 instead of G228 and D229.

Vertical cell imaging by nanostructured immobilization (VerCINI)

Overnight cultures were set up from a single colony in 2 ml M9 + glucose or LB and incubated at 37°C with orbital agitation at 175 rpm. The following morning, cultures were diluted to an OD₆₀₀ between 0.05 and 0.1 in 5 ml volumes then incubated at 30 or 37°C with orbital agitation at 175 rpm.

A VerCINI agarose pad was prepared by spotting 6% molten UltraPure agarose (VWR) dissolved in media onto a micropillar wafer and transferred into a Geneframe (Thermo Fisher Scientific) mounted on a glass slide as previously described⁴⁴. When cultures reached mid-exponential phase, at an OD₆₀₀ between 0.6 and 0.8, 500 µl of culture was centrifuged at 16,900 g for 1 minute then resuspended in 10 µl pre-warmed media. The 10 µl concentrated culture was spotted onto a pre-warmed VerCINI agarose pad. The slide was then centrifuged at 3,220 g for 4 minutes. The sample was then washed with pre-warmed media, to remove horizontal cells from the pad and air-dried, before a cover slip (VWR, 22 × 22 mm², thickness no. 1.5) was applied.

On a custom single-molecule microscope, samples were illuminated with 488 nm and 561 nm lasers (Obis) with a power density of ~ 17 W/cm² for 500 ms with HILO illumination⁶⁶ achieved by galvanometer-driven mirrors (Thorlabs) rotating at 200 Hz. A 100x TIRF objective (Nikon CFI Apochromat TIRF 100XC Oil), a 200 mm tube lens (Thorlabs TTL200) and a Prime BSI sCMOS camera (Teledyne Photometrics) were used for imaging, giving effective image pixel size of 65 nm/pixel. Images were denoised in Fiji⁶⁷ using the PureDenoise plugin⁶⁸.

Chemical fixation and immobilization

Chemical fixation and immobilization was performed as described previously²². Aliquots were taken at defined time points of drug treatment and fixed by directly adding fixation solution, providing a final concentration of 2% methanol-free formaldehyde (Thermo Fisher Scientific) and 0.2% EM-grade glutaraldehyde (Electron Microscopy Sciences) in 33 mM NaPO₄ buffer (pH 7.5). Cells were fixed for 12 min at room temperature (RT) and quenched by replacing the fixation solution with freshly made 0.2% NaBH₄ (Sigma Aldrich) in PBS for 3 min. Afterwards, cells were washed thrice with PBS and immobilized on KOH-cleaned (3 M KOH for 1 h), poly-L-lysine coated 8-well chamberslides (Sarstedt GmbH). All centrifugation steps were performed for 2 min at 6,000 g in a benchtop centrifuge (Thermo Fisher Scientific). For PAINT imaging, cells were permeabilized 30 min with 0.5% Triton-X-100 (Sigma Aldrich) and washed twice with PBS. 60 nm and 80 nm gold beads (Nanopartz Inc.) were added as fiducial markers at a concentration of 1:200 v/v each and allowed to settle for 30 min. Excess gold beads were removed by washing the well twice with PBS.

Click-labeling of metabolically labeled DNA

For the 3D measurement shown in Fig. 1A, cultures were grown as specified before except for adding 5-ethynyl-2-deoxyuridine (EdU, Baseclick GmbH) to the culture at OD₆₀₀ = 0.25 for 30 min. Cells were then fixed and immobilized as described above. Coupling with Alexa Fluor 647 azide (Thermo Fisher Scientific) was performed via copper-catalyzed click chemistry as described elsewhere³⁸. After the click reaction, cells were washed thoroughly with PBS and subjected to dSTORM imaging.

Confocal imaging of fixed cells

Immobilized cells were stained for DNA using 600 nM DAPI for 10 minutes. 100 nM Nile Red was added to the cells. As Nile Red is fluorogenic, samples were imaged without the removal of the staining solution. CLSM imaging was performed on a commercial LSM710 microscope (Zeiss, Germany) bearing a Plan-Apo 63x oil objective (1.4 NA). The internal 543 nm and 633 nm laser lines and an external LGN3001 argon-ion laser (LASOS Lasertechnik GmbH, Germany) were used as excitation light sources. A 405-100C Coherent Cube diode laser (Coherent GmbH, Germany) was additionally coupled into the microscope via an optical fiber. Suitable filter sets were chosen for each fluorescent probe. Triple-color measurements of NR-stained membrane, the GFP fusion protein and DAPI-stained chromosomal DNA were performed in sequential imaging mode following the indicated order to minimize photobleaching of GFP. Imaging was carried out using a pixel size of 84 nm, 16-bit image depth, 16.2 μ s pixel dwell time, 2x line averaging and 1 AU pinhole size. NR, GFP and DAPI were excited using 543 nm, 488 nm and 405 nm illumination, respectively. Fluorescent signal was detected at gains optimized for signal-to-noise ratio of each fluorophore. Emission detection windows were set to 547 – 753 nm, 492 – 541 nm and 409 – 542 nm for NR, GFP and DAPI, respectively in order to minimize crosstalk.

Live-cell imaging

Live-cell imaging was performed on a commercial Leica SP8 confocal microscopy (Leica Microsystems GmbH), equipped with a white-light laser and one hybrid detector. Cells were immobilized on agar

pads poured into gene frames⁶⁹ and imaged at room temperature. Dual-color imaging was performed in line sequential mode to reduce displacements caused by sample drift and the dynamic nature of the structures imaged. Obtained time series were denoised using PureDenoise⁶⁸ and corrected for photobleaching using the Fiji plugin “Bleach Correction” with histogram normalization.

Single-molecule localization microscopy

2D and 3D SMLM experiments were carried out on a custom build setup for single molecule detection or a commercial Nikon N-STORM system (Nikon Instruments). The custom-built system consists of a Nikon Ti-Eclipse body mounted with an 100x Apo TIRF oil objective (NA 1.49, Nikon Instruments), a perfect focus system (Ti-PFS; Nikon), a MCL Nano-Drive piezo stage (Mad City Labs), an adjustable TIRF mirror and a custom cylindrical lens for 3D imaging (RCX-39.0.38.0-5000.0-C-425-675, 10 m focal length, CVI Laser Optics, UK). An Innova 70 C Spectrum laser (Coherent) and a 405 nm UV diode laser (Coherent CubeTM 405-100C, Coherent) were used as excitation sources and laser lines were selected using an AOTFnC-VIS-TN acousto-optical tunable filter (AOTF, AA Opto Electronic). For dual-color PAINT imaging, 200 – 400 pM JF₆₄₆-Hoechst (DNA) and Nile Red (membrane) were added to the well in 150 mM tris pH 8.0²². Fluorophores were excited with 1 – 3 kW/cm² 561 and 647 nm laser light and image sequences were recorded in oblique illumination at frame rates between 33 and 50 Hz. 3D dSTORM imaging of click-labeled DNA (**Figure 1**) was performed in PBS containing 100 mM MEA (Sigma Aldrich), adjusted to pH 8.5 using NaOH.

Pseudo-3-color imaging

To co-image the nucleoid and membrane together with MreB and without chromatic aberrations, we imaged NO34 cells together with JF₅₀₃-Hoechst and Potomac Gold. Using a filter set that shows some crosstalk of these dyes in the 488 nm channel, DNA and subtle membrane signals are visible in the reconstructed image. MreB stacks were initially acquired using low laser intensity and subsequently bleached to facilitate single-molecule imaging of the transiently binding fluorophores.

Analysis of PAINT data

PAINT images of DNA and membranes were analysed using rapidSTORM v3.31⁷⁰. Binding events were fitted using a free parameter Gaussian fit with a threshold of 200 (JF₆₄₆-Hoechst) or 50 photons (Nile Red). Filtering was performed according to PSF width (JF₆₄₆-Hoechst: 240 nm < FWHM_{x/y} < 520 nm; Nile Red: 220 nm < FWHM_{x/y} < 440 nm) and symmetry (FWHM ratios between 0.7 and 1.3). Subsequent frame localizations were grouped into single localizations. Chromatic aberrations between channels were corrected using linear alignment matrices obtained from calibration images of fiducial markers, with the MreB channel serving as reference channel. Data for *Xenorhabdus doucetiae* was processed with Picasso⁷¹ using a similar routine.

Deconvolution of widefield MreB images

For deconvolution of the MreB channel, stacks with 100 nm spacing were recorded. Stacks were deconvolved with an experimental PSF obtained from fiducial markers (100 nm TetraSpeck microspheres, Thermo Fisher Scientific) using **Macro M1**. All macros used in this study are provided as Supplementary material and listed in **Table S3**. Multiple PSFs were extracted from the stack and averaged using a custom-written Fiji macro. Prior to deconvolution, MreB^{5W}-sfGFP stacks and the experimental PSF were scaled by a factor of 2 using bicubic interpolation. Stacks were deconvolved using the Fiji plugin ‘Parallel Iterative Deconvolution’.

Image registration

For registration of the different channels, cell outlines were extracted from smoothed super-resolved membrane PAINT images using a custom-written macro (**Macro M2**). MreB and DNA channels were manually translated into these outlines, minimizing the amount of signal outside the cell outlines.

Cell averaging (CLSM images)

Cell averaging was performed using custom-written Fiji macros. First, cells were segmented in the membrane channel of CLSM images and curated for cells that were only partially attached to the surface, as well as merged cells and debris. ROIs were saved and single cells were extracted using **Macro M3** according to the following routine: (i) Rotation according to the angle of a fitted ellipse. (ii) Straightening of the cells based on the centroids of 300 nm segments. (iii) Cell centering based on the center of mass. (iv) Normalization according to cell width and length by image rescaling to a fixed size using **Macro M4**. (v) Averaging using the Fiji tool 'Z-project'.

Measurement of the relative nucleoid length

Cell and nucleoid lengths were determined using the custom-written **Macro M5**. This analysis was performed on rotated, aligned and straightened cells, which were generated using **Macro M3**. The ratio of nucleoid and cell length finally provides the RNL.

Determination of the MreB intensity distribution

The relative MreB distribution to cell poles and the cell cylinder was quantified in CLSM average images (created in the previous section) using **Macro M6**. Cell poles and cylinder were defined using the membrane channel (Fig. S9) and respective ROIs were added to the RoiManager in Fiji. The relative intensity in the respective ROIs was calculated by equation 1,

$$I_{rel} = \frac{I_{ROI}}{I_{total}} \times \frac{Area_{total}}{Area_{ROI}} \quad (1)$$

where I_{rel} represents the relative intensity, I_{ROI} the integrated intensity in the selected ROI (either cell poles or cell cylinder), I_{total} the sum of the integrated intensities of pole and cylinder regions, $Area_{total}$ the sum of the respective areas and $Area_{ROI}$ the area of the selected ROI. Error analysis was performed using error propagation according to equation 2,

$$\Delta I_{rel} = \sqrt{\left(\frac{Area_{total}}{Area_{ROI}}\right)^2 \times \left(\left(\frac{1}{I_{total}}\right)^2 \times \Delta I_{ROI}^2 + \left(\frac{I_{ROI}}{I_{total}^2}\right)^2 \times \Delta I_{total}^2\right)} \quad (2)$$

where ΔI_{rel} represents the standard error of the mean (SEM) of I_{rel} , ΔI_{ROI} the SEM of I_{ROI} and ΔI_{total} the SEM of I_{total} . ΔI_{ROI} and ΔI_{total} were measured in standard deviation images created during the averaging procedure.

Determination of the radial intensity distribution (RID) in SMLM images

Bacterial outlines were smoothed and selected based on the Nile Red channel of multichannel SMLM images (**Macro M2**). The resulting ROIs were converted into a binary mask and masks of individual *E. coli* cells were eroded iteratively, radially reducing the binary mask in 40 nm steps (cell diameter hence shrinks by 80 nm per step). Resulting areas were transferred to the RoiManager and the integrated intensity in each ROI was measured both in the Nile Red membrane and JF₆₄₆-Hoechst DNA channel.

Erosion and intensity measurements were performed using **Macro M7**. The relative signal intensity I_{rel} in the removed area was calculated by equation 3,

$$I_{rel} = \frac{I_N - I_{N+1}}{I_{total}} \quad (32)$$

with I_N representing the integrated intensity of a bacterial section N , I_{N+1} the integrated intensity of the consecutive section created by erosion of N and I_{total} the integrated intensity within the whole bacterial outline. The relative area was determined by normalising the area of each ROI created by the erosion procedure (not the removed area) to the total area of the cell outline. Results for each erosion step were determined automatically and saved as text file. Data was finally plotted and visualised using OriginPro 9.1G (OriginLabs).

Determination of RID centre of mass and FWHM

The centres of mass and FWHM values for all time points and conditions were extracted from RID plots using the integration tool in OriginPro 9.1G.

Measurement of intensity plots in population averages

Intensity line plots were generated in population averages in Fiji by averaging the signal for the entire image width (cross-axis plots) or image height (length-axis plot). Standard deviations were extracted similarly from standard deviation images created during the averaging procedure. Intensity traces were further processed in OriginPro 9.1G.

Circular cross-correlation

Intensity traces of DNA and MreB signal were extracted from the triple-color images based on the cell outlines using **Macro M8**. In order to measure the signal close to the membrane, cell outlines were eroded by 20 px and signal was measured along the perimeter with a line width of 30 px. Circular cross-correlation was then calculated in Fourier space using z-score normalized data. For each condition, the cross-correlations for shift distances of -2 μm to 2 μm were averaged and plotted together with the standard error of the mean. The notebook for circular cross-correlation is provided as Supplementary Material and can be found in the Github repository (https://github.com/CKSpahn/Bacterial_image_analysis).

Simulation of images

To validate the circular cross-correlation approach, we simulated 3-color images using the custom-written Fiji macro **Macro 9**. We simulated a circle (membrane signal). 8 or 12 spots were positioned equidistantly and slightly towards the circle centre to mimic signals of MreB assemblies and DNA. Images were blurred using a Gaussian with a sigma of 4 pixels. To modulate the cross-correlation, MreB and DNA spots were shifted with respect to each other and intensity profiles of simulated images were extracted using **Macro M8**.

Training the model to segment DNA in SMLM images

For segmentation of super-resolved DNA in PAINT images, a content-aware image restoration (CARE) model was trained using the ZeroCostDL4Mic platform^{72,73}. A deep learning model is beneficial as single-molecule data has a lot of noise, coming from false-positive localizations, but images are also

not always homogeneously excited. To generate a model for DNA segmentation, we annotated images of bacteria treated with different antibiotics for different durations. For this, patches of reconstructed images were segmented manually using Fiji and ground-truth masks and image patches were saved separately. The CARE model was then trained on 50 annotated images for 100 epochs with a patch size of 256 x 256 px², 4 patches per image, a batch size of 4, 4-fold data augmentation, 332 steps per epoch, 10% validation data split and an initial learning rate of 0.0004. The prediction of the model was thresholded in Fiji using Otsu's method and DNA-populated area was measured within the cell outlines provided by membrane PAINT images. The trained model is available within the DeepBacs collection on Zenodo (**Table S4**).

ACKNOWLEDGEMENTS

C.S. and M.H. acknowledge funding by the Deutsche Forschungsgemeinschaft (German Research Foundation; DFG), grants HE 6166/17-1 and SFB 1507. C.S. further acknowledges support by the European Molecular Biology Organization (EMBO) in form of a Scientific Exchange Grant (grant nr. 8587). H.B.B. and C.S. acknowledge funding by the Max-Planck Society. R.H. and E.G.M. acknowledge the support of the Gulbenkian Foundation (Fundação Calouste Gulbenkian), the European Research Council (ERC) under the European Union's Horizon 2020 research and innovation programme (grant agreement No. 101001332) and the European Commission through the Horizon Europe program (AI4LIFE project with grant agreement 101057970-AI4LIFE, and RT-SuperES project with grant agreement 101099654-RT-SuperES), the European Molecular Biology Organization (EMBO) Installation Grant (EMBO-2020-IG-4734 to R.H.) and Postdoctoral Fellowship (EMBO ALTF 174-2022 to E.G.M.). This work is funded by the European Union. Views and opinions expressed are however those of the author(s) only and do not necessarily reflect those of the European Union. Neither the European Union nor the granting authority can be held responsible for them. SM was funded by a Biological Sciences Research Council (BBSRC) doctoral studentship (BB/M011186/1). SH acknowledges funding from a Wellcome Trust & Royal Society Sir Henry Dale Fellowship [206670/Z/17/Z]. C.S. and R.H. thank Ki Hng (Light microscopy facility at the LMCB, UCL, London) for assistance with the Zeiss Elyra PS1 system. We further kindly thank Zemer Gitai for providing the *E. coli* strain NO34. pmScarlet-i_C1 was a gift from Dorus Gadella (Addgene plasmid # 85044 ; <http://n2t.net/addgene:85044> ; RRID:Addgene_85044). pmMaple3-CAM was a gift from Xiaowei Zhuang (Addgene plasmid # 101148 ; <http://n2t.net/addgene:101148> ; RRID:Addgene_101148).

CONFLICT OF INTEREST

The authors declare no competing interests.

DATA AVAILABILITY STATEMENT

Confocal imaging data and multicolor super-resolution images for all conditions are available via Zenodo (**Table S4**). Custom-written macros and notebooks (**Table S3**) are provided as Supplementary Material and in our Github repository (https://github.com/CKSpahn/Bacterial_image_analysis). Single-molecule localization data is too large for public repositories and will be shared upon request.

REFERENCES

- 1 Reyes-Lamothe, R. & Sherratt, D. J. The bacterial cell cycle, chromosome inheritance and cell growth. *Nat Rev Microbiol* **17**, 467-478, doi:10.1038/s41579-019-0212-7 (2019).
- 2 Surovtsev, I. V. & Jacobs-Wagner, C. Subcellular Organization: A Critical Feature of Bacterial Cell Replication. *Cell* **172**, 1271-1293, doi:10.1016/j.cell.2018.01.014 (2018).
- 3 Reyes-Lamothe, R., Nicolas, E. & Sherratt, D. J. Chromosome replication and segregation in bacteria. *Annu Rev Genet* **46**, 121-143, doi:10.1146/annurev-genet-110711-155421 (2012).
- 4 Dame, R. T., Rashid, F. M. & Grainger, D. C. Chromosome organization in bacteria: mechanistic insights into genome structure and function. *Nat Rev Genet* **21**, 227-242, doi:10.1038/s41576-019-0185-4 (2020).
- 5 Dorman, C. J. Genome architecture and global gene regulation in bacteria: making progress towards a unified model? *Nat Rev Microbiol* **11**, 349-355, doi:10.1038/nrmicro3007 (2013).
- 6 Lioy, V. S. *et al.* Multiscale Structuring of the E. coli Chromosome by Nucleoid-Associated and Condensin Proteins. *Cell* **172**, 771-783 e718, doi:10.1016/j.cell.2017.12.027 (2018).
- 7 Youngren, B., Nielsen, H. J., Jun, S. & Austin, S. The multifork Escherichia coli chromosome is a self-duplicating and self-segregating thermodynamic ring polymer. *Genes Dev* **28**, 71-84, doi:10.1101/gad.231050.113 (2014).
- 8 Espeli, O., Mercier, R. & Boccard, F. DNA dynamics vary according to macrodomain topography in the E. coli chromosome. *Mol Microbiol* **68**, 1418-1427, doi:10.1111/j.1365-2958.2008.06239.x (2008).
- 9 Hadizadeh Yazdi, N., Guet, C. C., Johnson, R. C. & Marko, J. F. Variation of the folding and dynamics of the Escherichia coli chromosome with growth conditions. *Mol Microbiol* **86**, 1318-1333, doi:10.1111/mmi.12071 (2012).
- 10 Fisher, J. K. *et al.* Four-dimensional imaging of E. coli nucleoid organization and dynamics in living cells. *Cell* **153**, 882-895, doi:10.1016/j.cell.2013.04.006 (2013).
- 11 Marenduzzo, D., Finan, K. & Cook, P. R. The depletion attraction: an underappreciated force driving cellular organization. *J Cell Biol* **175**, 681-686, doi:10.1083/jcb.200609066 (2006).
- 12 Jun, S. & Mulder, B. Entropy-driven spatial organization of highly confined polymers: lessons for the bacterial chromosome. *Proc Natl Acad Sci U S A* **103**, 12388-12393, doi:10.1073/pnas.0605305103 (2006).
- 13 Wu, F. *et al.* Cell Boundary Confinement Sets the Size and Position of the E. coli Chromosome. *Curr Biol* **29**, 2131-2144 e2134, doi:10.1016/j.cub.2019.05.015 (2019).
- 14 Pelletier, J. *et al.* Physical manipulation of the Escherichia coli chromosome reveals its soft nature. *Proc Natl Acad Sci U S A* **109**, E2649-2656, doi:10.1073/pnas.1208689109 (2012).
- 15 Wu, L. J. *et al.* Geometric principles underlying the proliferation of a model cell system. *Nat Commun* **11**, 4149, doi:10.1038/s41467-020-17988-7 (2020).
- 16 Gray, W. T. *et al.* Nucleoid Size Scaling and Intracellular Organization of Translation across Bacteria. *Cell* **177**, 1632-1648 e1620, doi:10.1016/j.cell.2019.05.017 (2019).
- 17 Jin, D. J., Cagliero, C. & Zhou, Y. N. Role of RNA Polymerase and Transcription in the Organization of the Bacterial Nucleoid. *Chem Rev* **113**, 8662-8682, doi:10.1021/cr4001429 (2013).
- 18 Bakshi, S., Choi, H., Mondal, J. & Weisshaar, J. C. Time-dependent effects of transcription- and translation-halting drugs on the spatial distributions of the Escherichia coli chromosome and ribosomes. *Mol Microbiol* **94**, 871-887, doi:10.1111/mmi.12805 (2014).
- 19 Zimmerman, S. B. Toroidal nucleoids in Escherichia coli exposed to chloramphenicol. *J Struct Biol* **138**, 199-206, doi:10.1016/s1047-8477(02)00036-9 (2002).
- 20 Dworsky, P. & Schaechter, M. Effect of rifampin on the structure and membrane attachment of the nucleoid of Escherichia coli. *J Bacteriol* **116**, 1364-1374, doi:10.1128/jb.116.3.1364-1374.1973 (1973).
- 21 Spahn, C. *et al.* DeepBacs for multi-task bacterial image analysis using open-source deep learning approaches. *Commun Biol* **5**, 688, doi:10.1038/s42003-022-03634-z (2022).

- 22 Spahn, C. K. *et al.* A toolbox for multiplexed super-resolution imaging of the E. coli nucleoid and membrane using novel PAINT labels. *Sci Rep-Uk* **8**, doi:10.1038/s41598-018-33052-3 (2018).
- 23 Chai, Q. *et al.* Organization of ribosomes and nucleoids in Escherichia coli cells during growth and in quiescence. *J Biol Chem* **289**, 11342-11352, doi:10.1074/jbc.M114.557348 (2014).
- 24 Nonejuie, P., Burkart, M., Pogliano, K. & Pogliano, J. Bacterial cytological profiling rapidly identifies the cellular pathways targeted by antibacterial molecules. *Proc Natl Acad Sci U S A* **110**, 16169-16174, doi:10.1073/pnas.1311066110 (2013).
- 25 Zoffmann, S. *et al.* Machine learning-powered antibiotics phenotypic drug discovery. *Sci Rep* **9**, 5013, doi:10.1038/s41598-019-39387-9 (2019).
- 26 Zagajewski, A. *et al.* Deep Learning and Single Cell Phenotyping for Rapid Antimicrobial Susceptibility Testing. *medRxiv*, 2022.2012.2008.22283219, doi:10.1101/2022.12.08.22283219 (2022).
- 27 Wang, X. D., Brandao, H. B., Le, T. B. K., Laub, M. T. & Rudner, D. Z. Bacillus subtilis SMC complexes juxtapose chromosome arms as they travel from origin to terminus. *Science* **355**, 524-527, doi:10.1126/science.aai8982 (2017).
- 28 Weber, S. C., Spakowitz, A. J. & Theriot, J. A. Bacterial chromosomal loci move subdiffusively through a viscoelastic cytoplasm. *Phys Rev Lett* **104**, 238102, doi:10.1103/PhysRevLett.104.238102 (2010).
- 29 Xiang, Y. *et al.* Interconnecting solvent quality, transcription, and chromosome folding in Escherichia coli. *Cell* **184**, 3626-3642 e3614, doi:10.1016/j.cell.2021.05.037 (2021).
- 30 Nyathi, Y., Wilkinson, B. M. & Pool, M. R. Co-translational targeting and translocation of proteins to the endoplasmic reticulum. *Biochim Biophys Acta* **1833**, 2392-2402, doi:10.1016/j.bbamcr.2013.02.021 (2013).
- 31 Proshkin, S., Rahmouni, A. R., Mironov, A. & Nudler, E. Cooperation Between Translating Ribosomes and RNA Polymerase in Transcription Elongation. *Science* **328**, 504-508, doi:10.1126/science.1184939 (2010).
- 32 Matsumoto, K., Hara, H., Fishov, I., Mileykovskaya, E. & Norris, V. The membrane: transertion as an organizing principle in membrane heterogeneity. *Front Microbiol* **6**, 572, doi:10.3389/fmicb.2015.00572 (2015).
- 33 Woldringh, C. L. The role of co-transcriptional translation and protein translocation (transertion) in bacterial chromosome segregation. *Mol Microbiol* **45**, 17-29, doi:10.1046/j.1365-2958.2002.02993.x (2002).
- 34 Wang, X. D., Llopis, P. M. & Rudner, D. Z. Organization and segregation of bacterial chromosomes. *Nat Rev Genet* **14**, 191-203, doi:10.1038/nrg3375 (2013).
- 35 Kaval, K. G. *et al.* Membrane-localized expression, production and assembly of Vibrio parahaemolyticus T3SS2 provides evidence for transertion. *Nature Communications* **14**, doi:10.1038/s41467-023-36762-z (2023).
- 36 Sauer, M. & Heilemann, M. Single-Molecule Localization Microscopy in Eukaryotes. *Chem Rev* **117**, 7478-7509, doi:10.1021/acs.chemrev.6b00667 (2017).
- 37 Lelek, M. *et al.* Single-molecule localization microscopy. *Nat Rev Methods Primers* **1**, doi:10.1038/s43586-021-00038-x (2021).
- 38 Spahn, C., Endesfelder, U. & Heilemann, M. Super-resolution imaging of Escherichia coli nucleoids reveals highly structured and asymmetric segregation during fast growth. *Journal of Structural Biology* **185**, 243-249, doi:10.1016/j.jsb.2014.01.007 (2014).
- 39 Hardo, G., Li, R. & Bakshi, S. Quantitative Microbiology with Microscopy: Effects of Projection and Diffraction. *bioRxiv*, 2023.2005.2015.540883, doi:10.1101/2023.05.15.540883 (2023).
- 40 Spahn, C., Grimm, J. B., Lavis, L. D., Lampe, M. & Heilemann, M. Whole-Cell, 3D, and Multicolor STED Imaging with Exchangeable Fluorophores. *Nano Lett* **19**, 500-505, doi:10.1021/acs.nanolett.8b04385 (2019).

- 41 Libby, E. A., Roggiani, M. & Goulian, M. Membrane protein expression triggers chromosomal locus repositioning in bacteria. *Proc Natl Acad Sci U S A* **109**, 7445-7450, doi:10.1073/pnas.1109479109 (2012).
- 42 Ouzounov, N. *et al.* MreB Orientation Correlates with Cell Diameter in Escherichia coli. *Biophys J* **111**, 1035-1043, doi:10.1016/j.bpj.2016.07.017 (2016).
- 43 Whitley, K. D. *et al.* FtsZ treadmilling is essential for Z-ring condensation and septal constriction initiation in Bacillus subtilis cell division. *Nature Communications* **12**, doi:10.1038/s41467-021-22526-0 (2021).
- 44 Whitley, K. D., Middlemiss, S., Jukes, C., Dekker, C. & Holden, S. High-resolution imaging of bacterial spatial organization with vertical cell imaging by nanostructured immobilization (VerCINI). *Nat Protoc* **17**, 847-869, doi:10.1038/s41596-021-00668-1 (2022).
- 45 Takacs, C. N. *et al.* MreB drives de novo rod morphogenesis in Caulobacter crescentus via remodeling of the cell wall. *J Bacteriol* **192**, 1671-1684, doi:10.1128/JB.01311-09 (2010).
- 46 Lee, T. K. *et al.* A dynamically assembled cell wall synthesis machinery buffers cell growth. *Proc Natl Acad Sci U S A* **111**, 4554-4559, doi:10.1073/pnas.1313826111 (2014).
- 47 Cabrera, J. E., Cagliero, C., Quan, S., Squires, C. L. & Jin, D. J. Active transcription of rRNA operons condenses the nucleoid in Escherichia coli: examining the effect of transcription on nucleoid structure in the absence of transertion. *J Bacteriol* **191**, 4180-4185, doi:10.1128/JB.01707-08 (2009).
- 48 Hussain, S. *et al.* MreB filaments align along greatest principal membrane curvature to orient cell wall synthesis. *Elife* **7**, doi:10.7554/eLife.32471 (2018).
- 49 Kawazura, T. *et al.* Exclusion of assembled MreB by anionic phospholipids at cell poles confers cell polarity for bidirectional growth. *Molecular Microbiology* **104**, 472-486, doi:10.1111/mmi.13639 (2017).
- 50 Spahn, C., Cella-Zannacchi, F., Endesfelder, U. & Heilemann, M. Correlative super-resolution imaging of RNA polymerase distribution and dynamics, bacterial membrane and chromosomal structure in Escherichia coli. *Methods Appl Fluores* **3**, doi:10.1088/2050-6120/3/1/014005 (2015).
- 51 Sharonov, A. & Hochstrasser, R. M. Wide-field subdiffraction imaging by accumulated binding of diffusing probes. *P Natl Acad Sci USA* **103**, 18911-18916, doi:10.1073/pnas.0609643104 (2006).
- 52 Govindarajan, S. & Amster-Choder, O. The bacterial Sec system is required for the organization and function of the MreB cytoskeleton. *Plos Genet* **13**, doi:10.1371/journal.pgen.1007017 (2017).
- 53 Cabrera, J. E., Cagliero, C., Quan, S., Squires, C. L. & Jin, D. J. Active Transcription of rRNA Operons Condenses the Nucleoid in Escherichia coli: Examining the Effect of Transcription on Nucleoid Structure in the Absence of Transertion. *Journal of Bacteriology* **191**, 4180-4185, doi:10.1128/Jb.01707-08 (2009).
- 54 Vo, T. D., Spahn, C., Heilemann, M. & Bode, H. B. Microbial Cationic Peptides as a Natural Defense Mechanism against Insect Antimicrobial Peptides. *Acs Chemical Biology* **16**, 447-451, doi:10.1021/acscchembio.0c00794 (2021).
- 55 Diekmann, R. *et al.* Nanoscopy of bacterial cells immobilized by holographic optical tweezers. *Nature Communications* **7**, doi:10.1038/ncomms13711 (2016).
- 56 Wasim, A., Bera, P. & Mondal, J. On the Spatial Positioning of Ribosomes around chromosome in E. coli Cytoplasm. *bioRxiv*, 2023.2007.2004.547709, doi:10.1101/2023.07.04.547709 (2023).
- 57 Moffitt, J. R., Pandey, S., Boettiger, A. N., Wang, S. Y. & Zhuang, X. W. Spatial organization shapes the turnover of a bacterial transcriptome. *Elife* **5**, doi:10.7554/eLife.13065 (2016).
- 58 Nevo-Dinur, K., Nussbaum-Shochat, A., Ben-Yehuda, S. & Amster-Choder, O. Translation-independent localization of mRNA in E. coli. *Science* **331**, 1081-1084, doi:10.1126/science.1195691 (2011).

- 59 Liu, Z. *et al.* Super-resolution imaging and tracking of protein-protein interactions in sub-diffraction cellular space. *Nat Commun* **5**, 4443, doi:10.1038/ncomms5443 (2014).
- 60 Defeu Soufo, H. J. *et al.* Bacterial translation elongation factor EF-Tu interacts and colocalizes with actin-like MreB protein. *Proc Natl Acad Sci U S A* **107**, 3163-3168, doi:10.1073/pnas.0911979107 (2010).
- 61 Kruse, T. *et al.* Actin homolog MreB and RNA polymerase interact and are both required for chromosome segregation in Escherichia coli. *Genes Dev* **20**, 113-124, doi:10.1101/gad.366606 (2006).
- 62 Datsenko, K. A. & Wanner, B. L. One-step inactivation of chromosomal genes in Escherichia coli K-12 using PCR products. *Proc Natl Acad Sci U S A* **97**, 6640-6645, doi:10.1073/pnas.120163297 (2000).
- 63 Bindels, D. S. *et al.* mScarlet: a bright monomeric red fluorescent protein for cellular imaging. *Nat Methods* **14**, 53-56, doi:10.1038/nmeth.4074 (2017).
- 64 Wang, S., Moffitt, J. R., Dempsey, G. T., Xie, X. S. & Zhuang, X. Characterization and development of photoactivatable fluorescent proteins for single-molecule-based superresolution imaging. *Proc Natl Acad Sci U S A* **111**, 8452-8457, doi:10.1073/pnas.1406593111 (2014).
- 65 Philippe, N., Alcaraz, J. P., Coursange, E., Geiselmann, J. & Schneider, D. Improvement of pCVD442, a suicide plasmid for gene allele exchange in bacteria. *Plasmid* **51**, 246-255, doi:10.1016/j.plasmid.2004.02.003 (2004).
- 66 Tokunaga, M., Imamoto, N. & Sakata-Sogawa, K. Highly inclined thin illumination enables clear single-molecule imaging in cells. *Nat Methods* **5**, 159-161, doi:10.1038/nmeth1171 (2008).
- 67 Schindelin, J. *et al.* Fiji: an open-source platform for biological-image analysis. *Nat Methods* **9**, 676-682, doi:10.1038/nmeth.2019 (2012).
- 68 Luisier, F., Blu, T. & Unser, M. Image denoising in mixed Poisson-Gaussian noise. *IEEE Trans Image Process* **20**, 696-708, doi:10.1109/TIP.2010.2073477 (2011).
- 69 de Jong, I. G., Beilharz, K., Kuipers, O. P. & Veening, J. W. Live Cell Imaging of Bacillus subtilis and Streptococcus pneumoniae using Automated Time-lapse Microscopy. *J Vis Exp*, doi:10.3791/3145 (2011).
- 70 Wolter, S. *et al.* rapidSTORM: accurate, fast open-source software for localization microscopy. *Nat Methods* **9**, 1040-1041, doi:10.1038/nmeth.2224 (2012).
- 71 Schnitzbauer, J., Strauss, M. T., Schlichthaerle, T., Schueder, F. & Jungmann, R. Super-resolution microscopy with DNA-PAINT. *Nat Protoc* **12**, 1198-1228, doi:10.1038/nprot.2017.024 (2017).
- 72 von Chamier, L. *et al.* Democratising deep learning for microscopy with ZeroCostDL4Mic. *Nat Commun* **12**, 2276, doi:10.1038/s41467-021-22518-0 (2021).
- 73 Weigert, M. *et al.* Content-aware image restoration: pushing the limits of fluorescence microscopy. *Nat Methods* **15**, 1090-1097, doi:10.1038/s41592-018-0216-7 (2018).